MATERIALS SCIENCE

Electrophoretic digital colorimetry integrated with electrochemical sweat sensor

Daeun Sung[1], Seunghun Han[1,2], Sumin Kim[1,2], Heeseok Kang[3], Bon Jekal[1,2], Giheon Kim[1,2], Jaewon Kim[1,2], Minki Hong[1,2], Gyounghwan Moon[1], Sungeun Kim[1,2], Yerim Lee[1,2], Suk-Won Hwang[3,4,5], Hyoyoung Jeong[6], Yong-Sang Ryu[1,7,8], Sungbong Kim[9], Jahyun Koo[1,2]*

Recent advancements in wearable sweat sensors, which use standardized electrochemical and colorimetric mechanisms, offer holistic representation of health status for users. However, the constraints of standardized sweat sensors present ongoing challenges to realization of personalized health management. This study presents an electrocolorimetric (EC) platform that enables the reversible and multiple-time use of colorimetric data visualization using electrophoretic display (EPD). This platform represents the application of low-power EPD in epidermal sweat sensor, evaluated through CIELAB-based methodology which is the first systematic evaluation tool of wearable display performance. Moreover, our platform has been demonstrated in human exercise trials for its ability to detect the lactate threshold (LT). This digital colorimetric system has the potential to play a pivotal role by integrating various health monitoring biomarkers. While providing real-time, continuous, and adjustable range information with high sensitivity, this platform validates its extensive probability as a next-generation wearable epidermal sensor.

INTRODUCTION

Interest in wearable biosensors that have capabilities of diagnosis and health monitoring is continuously growing, and progress of the wearable sweat sensors integrating microfluidics to collect and analyze sweats is remarkable (*1*–*6*). These sensors detect various substances in sweat, revealing physiological information (*7*–*13*) and enabling applications in diagnosis of cystic fibrosis (*10*, *14*), assessing kidney function (*15*, *16*), evaluating stress (*3*, *17*), and perspiration dynamics (*15*, *18*, *19*). Furthermore, recent advancements integrating microfluidics and microelectronics have enabled devices to monitor both sweat composition and vital signs, such as heart rate and blood pressure (*20*, *21*), providing more holistic diagnosis of hypoglycemia, hyperglycemia, diabetes, and septic shock (*20*, *22*). These efforts overcome the limitation of conventional sweat research methods that use gauze pads (*23*) and expand toward nondiscovered area such as iontophoresis of perspiration-inducing drugs for the patients who have mobility issues (seniors and pregnancy) (*24*, *25*).

Sweat sensors primarily use electrochemical or colorimetric sensing mechanisms for quantitative analysis (*2*, *23*). Each mechanism has its own distinct features and specific challenges. Electrochemical sensors convert the concentration of the substrate into an analog signal (e.g., current) that can be further converted into digital signals (*1*, *5*, *7*–*9*, *12*, *13*, *16*, *18*, *20*, *21*). Electrochemistry offers high sensitivity and fast response upon which the microfluidic geometries confine reactions to specific spaces. However, a comprehensive electrode system with additional electrode modification needs to be integrated, along with electronics for data processing. As a result, the packaging of these components often leads to bulkier devices, and sometimes heavy instruments are required to analyze clinical data. Colorimetric sensors use chemical and/or enzymatic reactions to produce color changes (*3*, *10*, *26*–*34*). The developed color intensity is proportional to the amount of the substrate in sweat. Colorimetric sensors have on-the-spot perceptibility, user-friendliness (i.e., simplicity and ease of use), and portability with miniaturized device size. Their primary limitation arises from their reliance on specific colorimetric reactions as the core principle. Sometimes, the ranges of biomarkers and the reactive spectrum of colorimetric reactions may not align well with physiological conditions (*10*, *35*). Consequently, achieving fully multiplexed biosensing solely based on colorimetric sensing remains challenging. These limitations of both mechanisms create substantial barriers to the usability of wearable devices in personalized health management. For instance, the substantial size of electrochemical devices and their analytical instruments reduces practical accessibility, as they increase the burden on long-term wear or monitoring in various environments for users. In addition, the physiological mismatch in colorimetric sensing limits their ability to provide holistic and comprehensive health monitoring.

In this context, recent strategies in wearable sensing platforms use existing display technologies integrated with biosensing mechanisms. Electrochromic display (ECD), which shows visible color change through redox reactions (*36*, *37*), has demonstrated its ability to colorimetrically display real-time health care information on biomarker concentrations, strain, and temperature without the need for bulky external instruments (*1*, *38*–*41*). In addition, electrophoretic display (EPD), which leverages the movement of light-reflective pigments within a dyed colloidal solution under an electric field (*42*, *43*), is being widely researched for its high ambient visibility and contrast, making it ideal for flexible, on-skin displays (*44*, *45*).

[1]School of Biomedical Engineering, Korea University, Seoul 02841, Republic of Korea. [2]Interdisciplinary Program in Precision Public Health, Korea University, Seoul 02841, Republic of Korea. [3]KU-KIST Graduate School of Converging Science and Technology, Korea University, 145 Anam-ro, Seongbuk-gu, Seoul 02841, Republic of Korea. [4]Center for Biomaterials, Biomedical Research Institute, Korea Institute of Science and Technology (KIST), Seoul 02792, Republic of Korea. [5]Department of Integrative Energy Engineering, Korea University, Seoul 02841, Republic of Korea. [6]Department of Electrical and Computer Engineering, University of California, Davis, CA 95616, USA. [7]Department of Micro/Nano Systems, Korea University, Seoul 02841, Republic of Korea. [8]BK21 Four Institute of Precision Public Health, Korea University, Seoul, Republic of Korea. [9]Department of Chemistry, Korea Military Academy, Seoul 01805, Republic of Korea.
*Corresponding author. Email: jahyunkoo@korea.ac.kr

In this study, we aim to create a wearable sweat-sensing platform called electrocolorimetric (EC) platform, by combining electrochemical high sensitivity and colorimetric convenience strategies using EPD. The results of the electrochemical biosensing reaction are visualized by EPD. Because of the reversible migration of the pigments, the color development of EPD can be reset, allowing the system to exhibit multiple concentration levels of the substrates sequentially and continuously. The EC platform not only delivers sensor information through the EPD but also transmits numerical data via Bluetooth low energy (BLE). This dual data monitoring approach allows users to receive immediate feedback while enabling detailed analysis of stored data for future use. Moreover, the EPD operates efficiently at a low voltage of 3.3 V and requires only minimal current, making it highly suitable for integration into wearable devices. The systematic methodology for the quantitative analysis of wearable display is also presented, offering a comprehensive approach for the evaluation of the key features in wearable display including color, response time, and reliability. Our strategy using EPD highlights potential advantages compared to a strategy using ECD, featuring a fast response time and low-power consumption, comparable to or more efficient than ECD, while offering a simple, fast, and straightforward fabrication process that ensures high reproducibility (*46*, *47*). Human trials include measurement of lactate threshold (LT) to ensure the completed EC platform is available in situ. This helps determine the point of exercise intensity at which excessive muscle fatigue accumulates (*27*). The EC platform's approach, integrating electrochemical sensors and EPD, and its analytical methodology proposed here demonstrate its extensive practicality and applicability as a next-generation long-term wearable sensor.

RESULTS

EC sensing system

Figure 1A illustrates the concept and principle of the EC sensor, which consists of three interconnected components: the electrochemical sensing module, processing module, and colorimetric displaying module. The electrochemical signal calibrated by a pH value is processed in microcontroller unit (MCU) to control EPD array.

The electrochemical sensing module includes units for lactate and pH sensing, the latter aiding in the calibration of the electrochemical sensor (Fig. 1B, left). Lactate was selected to demonstrate the feasibility of the EC platform. It increases dynamically in sweat and blood at LT, a point where lactate production exceeds consumption, serving as an indicator of muscle fatigue and exercise intensity (*48*, *49*). Along with LT-based physical training for athletes, the possible clinical situation encompasses the quantification of exercise intensity customized for patients with cardiovascular disease and cerebrovascular accident in cardiac rehabilitation program, which contributes to reduced risk of death by 47% (*50*–*53*). For precise pH calibration, the RGB sensor assesses RGB values of pH paper in a microfluidic channel.

After the estimation of lactate level in processing module (Fig. 1B, middle), the "on" and "off" states of EPDs are displayed as low contrast (darker blue) and high contrast (brighter blue), respectively (Fig. 1B, right). White TiO_2 powder coated with charge-derived polymer {TiO_2/poly(methyl methacrylate)–ethylene glycol dimethacrylate–*co*–methacrylic acid [TiO_2/P(MMA-EGDMA)-*co*-MAA]} reflects light in both upper and lower positions in electronic-ink (E-ink) filled between electrode pair. A transparent indium tin oxide (ITO) electrode is located at the top in electrode pair of EPD unit, allowing the display unit to represent on state when the white pigment particles are placed below via E-field control. The voltage thresholds of on states in each EPD units correspond to lactate concentrations of 0, 5, 10, and 15 mM, labeled as lactate levels 1 to 4 (table S1). These thresholds were determined on the basis of previous human experiments, where the peak lactate concentration ranged from 10 to 20 mM (*5*, *27*, *54*, *55*). The lactate concentrations can be adjusted in the MCU module based on the specific application needs. The exercise intensity can be determined by both the lactate level displayed on the EPD array and a smartphone application. These accessibilities propose the capability of EC platform to overcome current limitations of LT estimation in cost, space, and time (*56*, *57*).

The EC device has a unique folded structure. It consists of a pair of electrodes: a copper layer on the flexible printed circuit board (FPCB) serving as the bottom electrode and a transparent ITO/glass connected to FPCB via Ag glue as the top electrode. This design enables the generation of a vertical E-field for EPD. The electrodes can be easily transformed from planar to vertical arrangement by folding, allowing them to generate the E-field. Figure 1C details the fabrication process, including EPD module implantation, folding and sensing module implantation, and E-ink injection. An elastomer mixture, a blend of polydimethylsiloxane (PDMS) and Dragon Skin at a ratio of 3:4, was used to establish EPD module which embeds ITO/glass and E-ink. This mixture ensures nonswelling of E-ink chamber and enables plasma bonding with the FPCB substrate (figs. S1 and S2). An Si wafer mold etched by deep reactive ion etching (DRIE) was used for precise alignment of ITO/glass top electrode with the elastomer mix (fig. S3). Following the EPD module's implantation, the sensing module was arranged on the EC device via plasma bonding, similar to the EPD module. Lastly, the E-ink suspension oil was injected into the E-ink chamber through preprepared inlets. The images of the EC sensor device (Fig. 1, D and E) demonstrates that it was sufficiently flexible to conform to human skin.

Enzymatic lactate sensing complemented by RGB calibration

A biofuel cell-based enzymatic sensing system was integrated into the EC platform by transferring electrodes to a FPCB substrate and enclosing them within a PDMS microfluidic chamber to facilitate sweat collection (Fig. 2A). As depicted in Fig. 2B, capillary bursting valves positioned at a 90° angle prevent the collected sweat from flowing into outlet channels until the sensing chamber is fully filled (fig. S6). The configuration of the cathode and the anode is shown in Fig. 2C. The reduction of O_2 and oxidation of lactate were catalyzed by platinum black (PtB) and lactate oxidase (LOx), respectively. Tetrathiafulvalene (TTF), chosen for its dermal compatibility and high sensitivity (*58*), served as the electron transfer mediator on the anode (fig. S7). TTF and LOx were immobilized on a carbon nanotube (CNT) paper, a highly conductive substrate that enhances electron transfer from the active site of LOx to the gold electrode. The scanning electron microscopy (SEM) images of bare CNT, TTR-CNT, and LOx-TTF-CNT illustrate the detailed nanostructural characteristics of the CNT-based anodes, where a homogeneous distribution is observed (fig. S8). Both the cathode and the anode were encapsulated with diffusion barriers—Nafion and polyvinyl chloride (PVC)—to provide an appropriate sensing range including physiological levels and prevent dissolution of the sensing layer. The circular sensitive

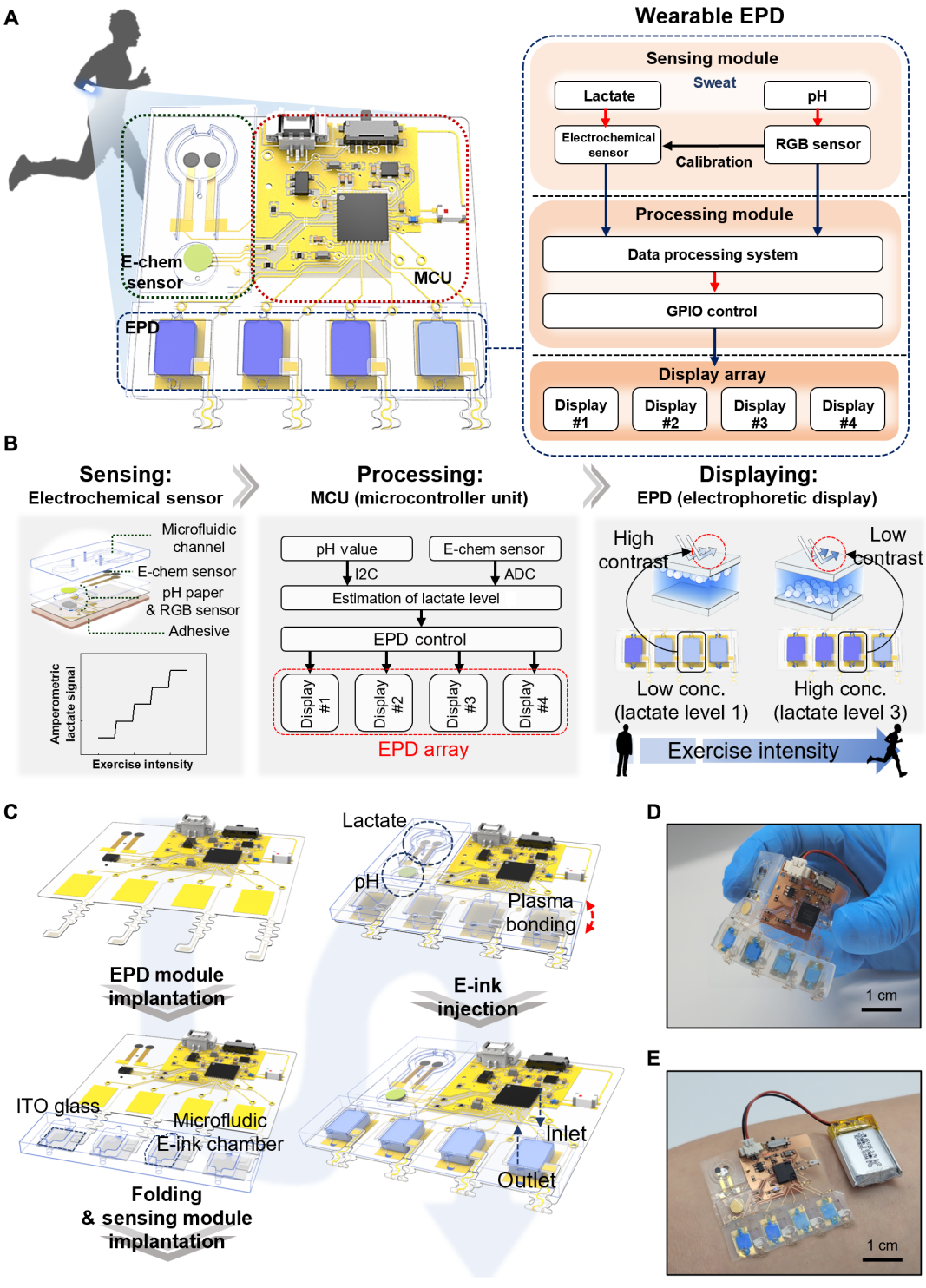

Fig. 1. Concept and principle of EC sensor. (**A**) Detailed overview of EC sensor divided into sensing, processing, and EPD module. (**B**) Operational principle of EC platform. Electrochemical sensor is in charge of lactate sensing that will be calibrated by RGB sensor. The detected concentration information is processed by MCU, resulting in the EPD array's displaying that represents lactate levels from 1 to 4 through the on/off state change. (**C**) Fabrication process of EC sensor characterized by a folded structure. (**D** and **E**) Images of EC sensor and its epidermal wear.

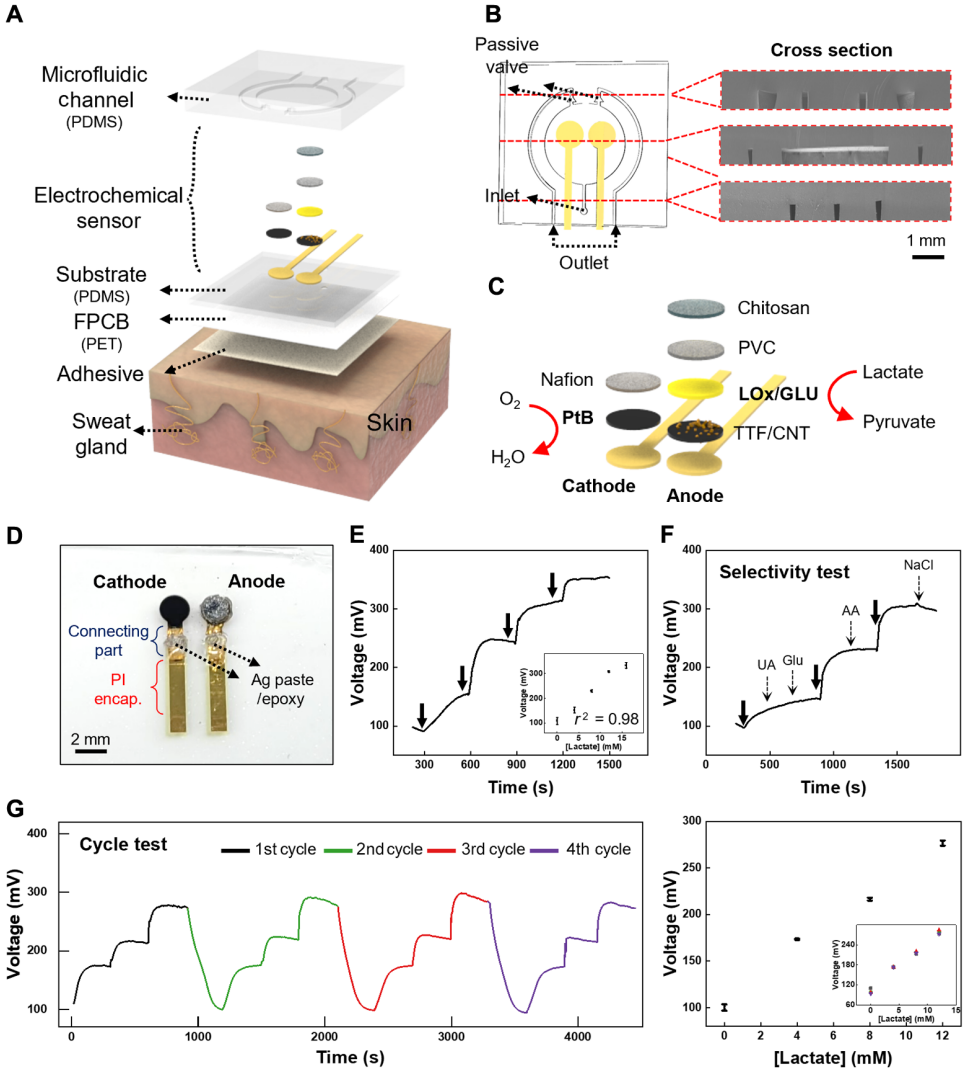

Fig. 2. Characterization of amperometric lactate sensor. (**A**) Exploded view of amperometric sensing module attached onto skin. (**B**) Microfluidic design for the sweat collection and its SEM image. (**C**) Configuration of anode and cathode. (**D**) Photographic image of cathode and anode. (**E**) Voltage response of amperometric sensor in phosphate buffer (pH 7.4, 37°C) and its calibration curve ($n = 4$). At each indicated time point, lactate was added by 4 mM. (**F**) Result of selectivity test conducted in the lactate concentration range from 4 to 12 mM. UA, uric acid; Glu, glucose; AA, ascorbic acid. (**G**) Result of cycle test for the amperometric sensor including four successive experiments (left) and its calibration curve (right). In the calibration curve, each data point represents the mean, and the error bars indicate the SD.

areas decorated with PtB or LOx were fabricated separately and connected to transferred rectangular electrodes using Ag paste (Fig. 2D).

The sensitivity and selectivity of the electrochemical sensor were tested in phosphate buffer at pH 7.4 and 37°C (Fig. 2, E and F). The amperometric response was converted to voltage signal using a 47-kilohm resistor, selected on the basis of the feasible linearity and fast response time. The r^2 values for the linear fit and response time offered by a 47-kilohm resistor were 0.9847 and 80.45 s, in order (fig. S9). The average response time of approximately 80.45 s was considered adequate as the composition of biofluid did not shift rapidly compared with benchtop conditions (*27*). A stable and saturated response time is anticipated in real human use. In the sensitivity test of amperometric lactate sensor (Fig. 2E), 4 mM concentrated lactate solution was added every 5 min, causing sharp stair-shaped increase in voltage from 109.236 mV at 0 mM to 332.97 mV at 16 mM. The selectivity of the sensor was also evaluated under similar conditions (Fig. 2F). An increase in voltage was observed only when lactate was introduced, while common sweat interferences such as uric acid (UA; 10 μM), glucose (100 μM), ascorbic acid (AA; 50 μM), and NaCl (10 mM) exhibited no effect on the signal. The cycle test of the sensor (Fig. 2G) showed that at least four response cycles were possible, with favorable recovery to the state of 0 mM. The standard errors (SEs) for voltage responses at each concentration were only 3.42, 0.65, 1.55, and 2.75 mV across the cycles.

The amperometric sensing system demonstrated a distinctive pH sensing system. The pH dependence of the amperometric sensor, due to the pH-dependent activity of LOx, proposes the necessity of this system (fig. S11). The pH value was accurately determined digitally by detecting the color of the pH paper using an RGB sensor with a white light-emitting diode (LED) even in different light environments. This notably improved the correlation between RGB values and pH levels (fig. S12 and table S2). This enhanced accuracy

allows for the further use of this simple setup to monitor pH-related clinical symptoms such as alkalosis or dehydration (*59*).

Processing module for dual visualization of EPD array and smartphone application

The processing module that controls the sensing module, general purpose input/output (GPIO) control, and wireless module enables a dual-visualization strategy for users to monitor health status simultaneously via the EPD array and smartphone application (Fig. 3A). The integration of the EPD array and a smartphone application provides an enhanced health care monitoring experience. The EPD is responsible for the instantaneous and intuitive delivery of health information, whereas the smartphone application tracks and assesses the overall trend of biomarker changes during perspiration even in a large group. This dual-displaying capability highlights the practical utility of the EC platform, particularly in specialized environments such as military and medical facilities, where continuous health monitoring is crucial for both individual and large group assessments.

In the wireless module, the custom-developed smartphone application receives data via a 2.4-GHz tuned antenna following the BLE protocol, displaying real-time graphs. For the EPD-controlling unit, the EPD array operates via eight GPIO of the MCU. The MCU classifies lactate molarity into four levels and determines the number of EPD units to be switched to on state (fig. S15). This switch is executed by applying a driving waveform to the electrodes via GPIO, facilitating rapid EPD activation every 200 ms. Our device is powered by a 3.7-V lithium polymer battery. With a power consumption of 18.374 mV/s (fig. S16), it can operate for approximately 11.97 hours using a conventional 220-mAh battery, making the EC platform well-suited for real-world applications.

Wearable epidermal electronics are subjected to potential bending forces that could affect their stable operation. A bending test confirmed the stability of this system's circuitry elements with bending radii ranging from 1 to 10.5 cm (Fig. 3B). Packet reception rate (PRR), the ratio of BLE packets transmitted by the processing unit to those received by the smartphone within a specific period, remained above 98% across the tested spectrum (Fig. 3C). In addition, the temperature of processing module was not excessively increased by whether the device operates or not in any temperature conditions (Fig. 3, D and E). PRR of processing module was evidently stable at the same time regardless of circumstantial temperature, as well as the distance between a transceiver and a receiver (fig. S17). These results proved the feasibility of EC sensor, allowing EC sensor to be used without any data loss and skin burn under various conditions.

Reliable EPD for wearable sensor

Figure 4A provides a detailed look at the configuration of the EPD array and how it operates. A notable observation is that surface charges are present not only on the pigment powders but also on the side walls surrounding the E-ink, which induces an E-field in unintended directions (Fig. 4A, bottom). The use of silicone-based materials in the display module, PDMS and Dragon Skin, exacerbates this issue as these materials tend to accumulate negative surface

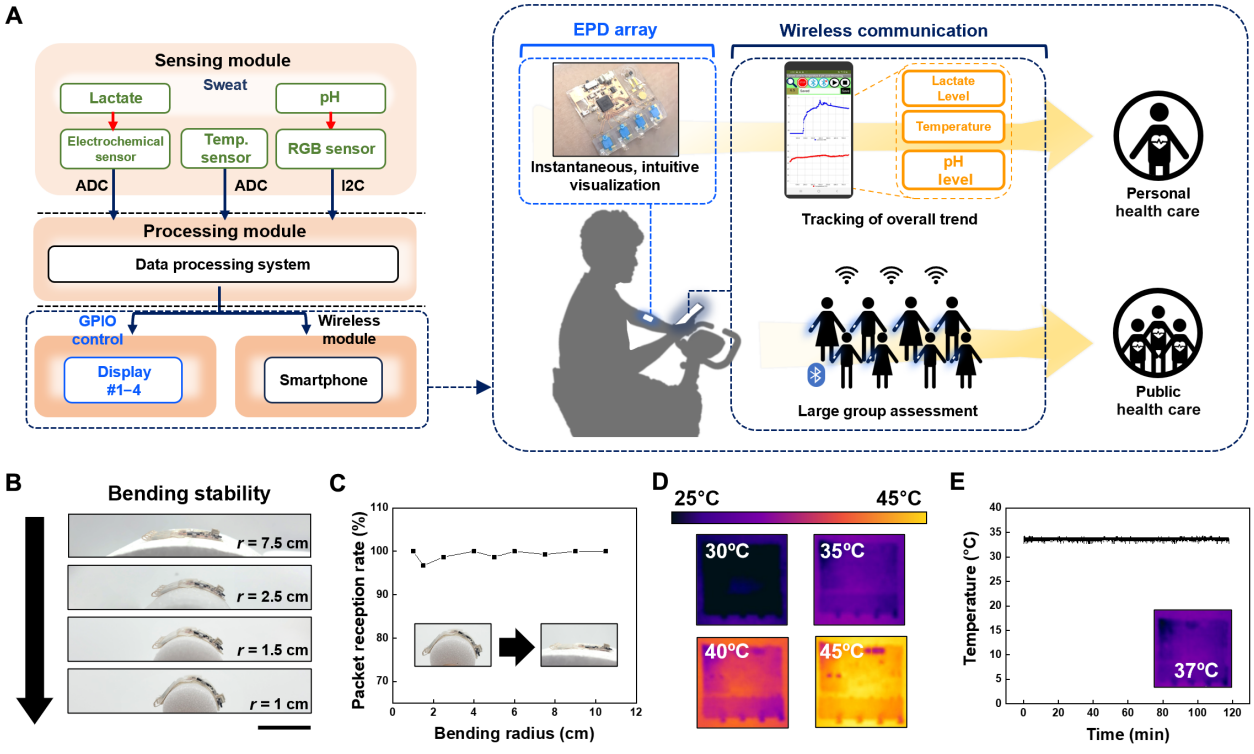

Fig. 3. Characterization of processing module. (**A**) Operational diagram of the processing module facilitating dual visualization of EPD array and smartphone application. (**B**) Optical images of devices that are bent to different bending radii. Scale bar, 2 cm. (**C**) PRR of processing module depending on varying bending radii (1 to 10.5 cm). (**D**) Infrared images of EC device in operation on various temperature of hot plate (30° to 45°C), in which no any excessively increased temperature was detected. (**E**) Temperature monitored in EC sensor when it operated on a hot plate (37°C).

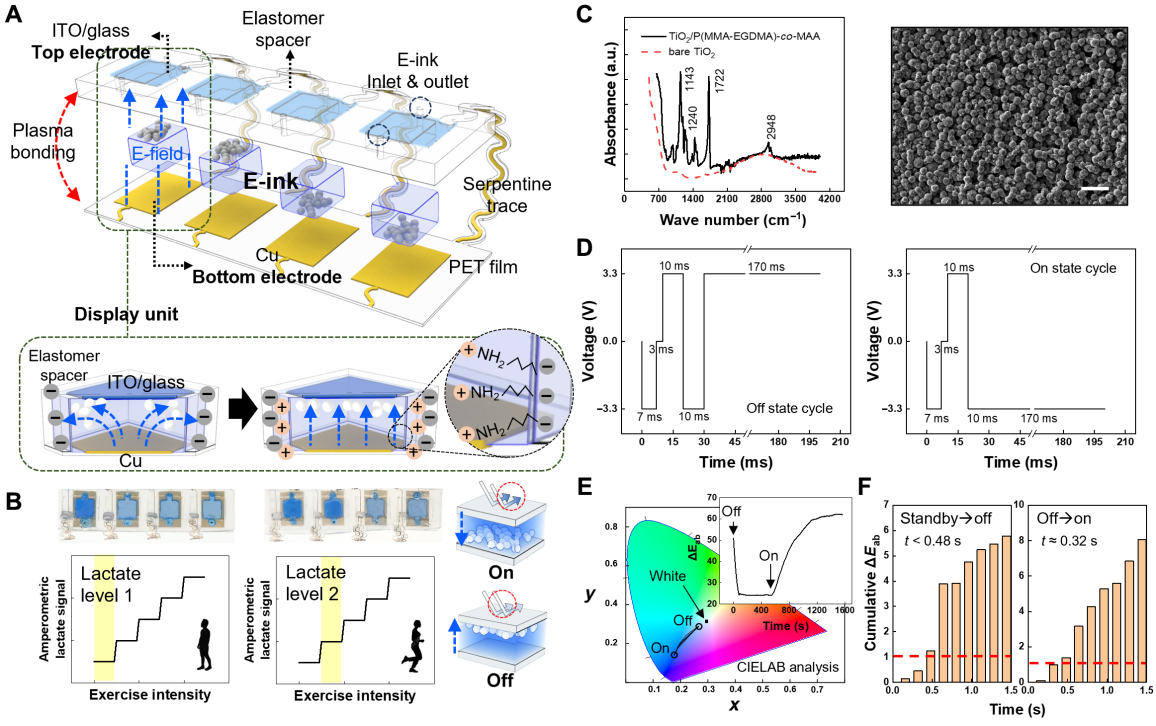

Fig. 4. Characterization of EPD. (**A**) Schematic image of EPD realized via folded structure of EC sensor (top) and enlarged illustration of EPD display unit of which surface was treated as -NH_2 to rectify a distorted E-field (bottom). (**B**) Configuration of the EPD system that can sequentially represent the lactate level and exercise intensity by changing the on/off state through the vertical movement of the white pigment. (**C**) FTIR analysis and SEM image of white pigment particles [TiO_2-P(MMA-EGDMA)-*co*-MAA]. Scale bar, 20 μm. (**D**) Driving waveforms of EPD for on/off state. (**E** and **F**) CIELAB analysis for the quantification of on/off state color of EPD. The color of EPD's on/off state was marked on CIEXYZ coordinates, and further calculated ΔE_{ab} was also plotted as the real-time color difference based on reference white color (E). Response time which is defined as the time taking for person to recognize the color difference ($\Delta E_{ab} > 1$) was estimated via cumulative ΔE_{ab} (F). a.u., arbitrary units.

charges owing to their high electron affinity (*60*). This characteristic stems from their ability to readily accept and retain electrons from the environment. To counteract this, a surface treatment using -NH_2 was used to minimize the distortion. By applying -NH_2, which imparts a positive charge to the surface of these materials, the surface charge is neutralized, thereby facilitating the formation of a desired vertical E-field between the electrodes. The effectiveness of the -NH_2 functionalization was quantitatively assessed using the Kelvin probe force microscopy mode in atomic force microscopy (AFM) and zeta potential measurements in a flat-cell configuration (fig. S18 and Supplementary Text). In both assessments, the increased surface potential after -NH_2 functionalization was quantified. Both AFM and zetasizer analyses demonstrate that -NH_2 functionalization effectively neutralizes the negative surface potential of the silicone elastomer by enhancing the surface potential.

To convey the user's exercise intensity properly (Fig. 4B), the white pigment particles moving vertically within the E-ink was chosen deliberately in consideration of their physical and optical properties such as high reflectance or dispersion stability. Meeting these requirements, TiO_2, known for its high reflectance ($n = 2.4116$), was functionalized with carboxyl groups to form a composite structure referred to as TiO_2/P(MMA-EGDMA)-*co*-MAA (fig. S19). This modification enables pigment particles to undergo swift electrophoretic displacements in E-field, characterized by the mobility equation $\mu = \epsilon\zeta / 6\pi\eta$ (*61*). Characterization of the TiO_2/P(MMA-EGDMA)-*co*-MAA pigment particles included Fourier transform infrared (FTIR) spectroscopy and SEM imaging (Fig. 4C). The FTIR spectra displayed notable peaks between 1143 and 1240 cm^{-1}, corresponding to the carbonyl group (C—O) of C—O—CH_3, and a distinct peak at 1722 cm^{-1} related to the carbonyl group (C═O) of the polymer (*62*, *63*). The SEM image of TiO_2/P(MMA-EGDMA)-*co*-MAA revealed a uniform spherical shape with a diameter of approximately 7 μm, showing an increase from 300 nm to 7 μm after synthesis without any aggregation (fig. S20). In further analysis using a gas pycnometer, the density of the particles was measured as 1.4420 g/cm^3 (SD = 0.0016 g/cm^3), sufficiently reduced from the initial 4.0350 g/cm^3 (SD = 0.0016 g/cm^3) to fabricate oil suspension whose density matched that of the pigment particles (fig. S21).

The driving waveform, applying ±3.3 V to induce on and off states, was optimized to produce a human-recognizable contrast change without blinking within a brief response time (Fig. 4D). Note that the driving waveform incorporated a "shaking phase," where E-fields in two vertical directions were applied rapidly to initialize the undesired, inevitable distribution of charged materials within the E-ink chamber.

The operation of EPD was appraised using CIELAB analysis, which examines color space irrespective of lighting conditions. The RGB parameters were converted to *x* and *y* parameters, and the change in color was represented as a line with unfilled circles indicating saturated colors of on and off states (Fig. 4E). The line representing the real-time color change radiates outward from the central point standing for "white," suggesting that the color of the dyed solution varies only based on the relative position of the white pigment. ΔE_{ab}, indicating the quantitative color difference in CIELAB,

was calculated likewise (Fig. 4E, inset) to reveal real-time color change when the applied driving waveform transitioned from the off state to the on state.

The response time was defined as the duration for cumulative ΔE_{ab} to exceed 1 (Fig. 4F). This threshold is based on established knowledge that $\Delta E_{ab} > 1$ is discernible by humans (*64*). The contrast transition involving $\Delta E_{ab} > 1$ took 0.48 s for the preparation to off state after "standby" state and 0.32 s for the conversion to on state from off state. The graph of cumulative ΔE_{ab} exhibited a steady and continuous increase without abrupt fluctuations. These results of CIELAB analysis are clearly distinguished from that of the samples without -NH_2 functionalization or the shaking phase in the driving waveform (figs. S22 and S23), demonstrating the efficacy of these strategies in practical EPD applications.

Human trial

EC devices were affixed to the foreheads of healthy volunteers engaged in a controlled exercise scenario (Fig. 5A). Before attaching the EC devices using biocompatible double-sided tape, volunteers' skin was cleaned with an alcohol wipe to minimize sweat contamination. Participants were instructed to avoid caffeine and alcohol for 24 hours before the experiment to ensure no interference with the test results (*65*). The volunteers performed a warm-up until noticeable perspiration occurred ($t = 0$). The EC devices were mounted at

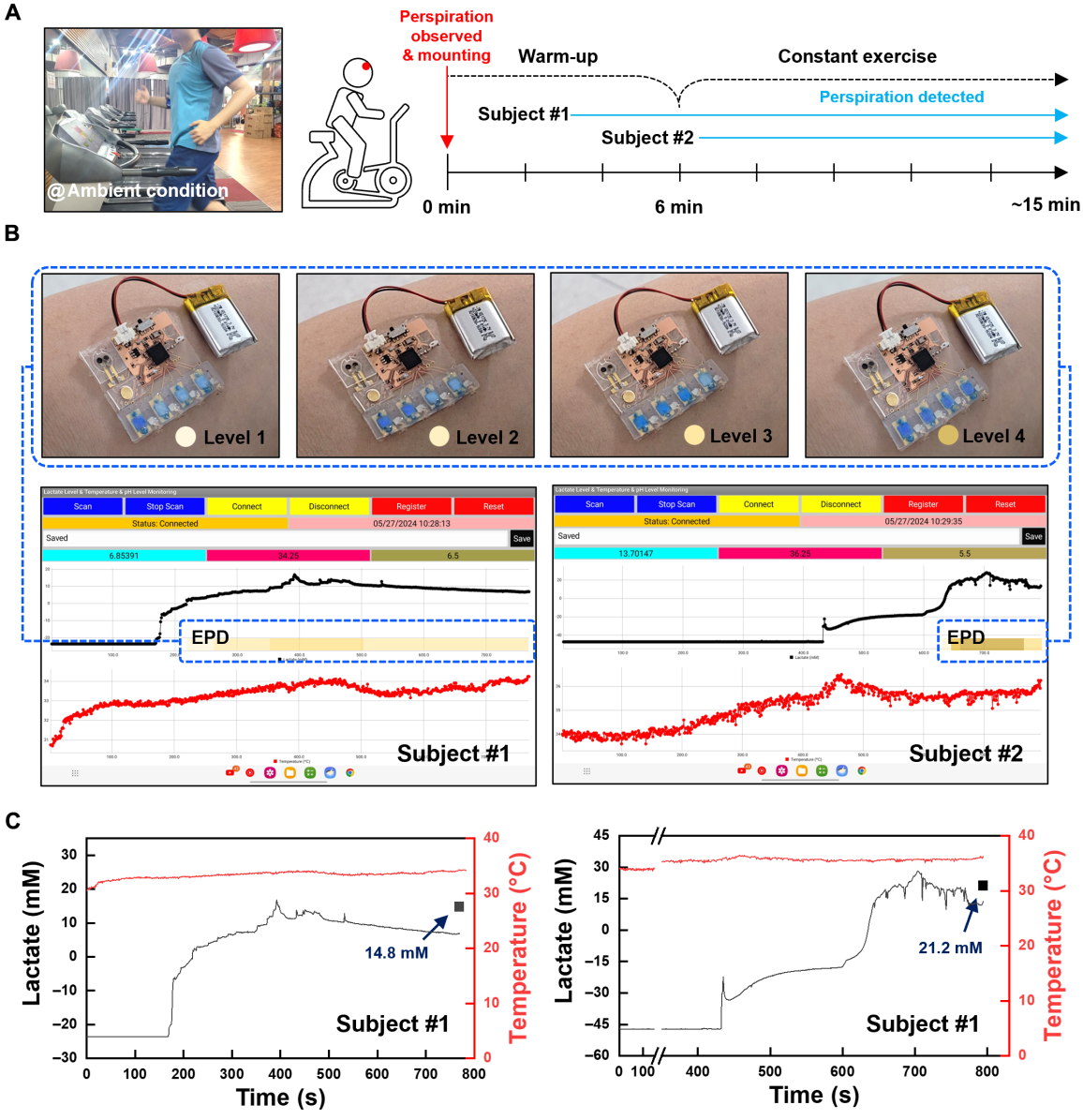

Fig. 5. Human trial. (**A**) Experimental scheme for healthy subject participation. The EC device was mounted onto the participant's forehead after perspiration observed ($t = 0$). (**B**) Photograph demonstrating lactate levels 1 to 4 displayed by the EC sensor, along with real-time measured sweat lactate concentration and temperature illustrated via a smartphone application. Measured lactate concentration and the corresponding EPD response are aligned (blue dotted line). (**C**) Postanalyzed lactate concentration and temperature data facilitated by the BLE system. Square dots represent lactate concentrations detected by a commercial sensor.

this initial point, and the warm-up continued for an additional 6 min. Subsequently, participants engaged in continuous exercise at an intensity designed to stimulate anaerobic metabolism and induce LT.

The on-body demonstration was conducted under ambient conditions, where each EPD unit was activated sequentially in response to increasing lactate concentrations, with the corresponding real-time concentration and temperature data simultaneously displayed on a smartphone application (Fig. 5B). The BLE system of the EC platform also facilitated postanalysis of trends, as illustrated in Fig. 5C. Notably, the noise levels remained low even under intense exercise conditions, which typically involve extensive movement. A sharp increase in the signal was detected, mirroring the response pattern observed in in vitro tests when additional lactate was introduced. This sharp rise in lactate concentration is attributed to increasing exercise duration and muscle fatigue. The lactate concentration after LT ranged from approximately 10 to 20 mM, aligning with findings from previous studies (*5*, *27*, *54*, *55*).

This system is distinctly differentiated from the existing colorimetric system. Multiple concentration levels of analytes are delivered sequentially and continuously with just one display array; therefore, no separate chambers are required. In addition, the MCU can set the range of concentration levels delivered by the EPD, enabling it to overcome the limitation of existing colorimetric reaction, which responds visibly only within a specific concentration range. The compatibility of wearable EPD with electrochemical sensors and FPCB, which are being commonly used in epidermal sensors, verifies the expandability of EC platforms.

DISCUSSION

We developed a wearable sweat sensor platform that integrates electrochemical and colorimetric mechanisms through the use of EPD technology. The MCU, as part of the data processing module, uniquely reads pH status using RGB sensor and digitally calibrates the electrochemical lactate signal to reflect the physical condition in both smartphone and EPD array. The wearable EPD was created using a unique folding structure that produces vertical E-field. The performance of the wearable EPD was further enhanced by chemical surface treatments and the optimization of driving waveform. The CIELAB method enabled the quantitative analysis of these enhancements. For the optimized EPD, we confirmed a response time of less than 0.5 s and a contrast difference of at least $\Delta E_{ab} > 30$. The human trial demonstrated the potential for the sensor to be used both holistically and personally, through the concurrent use of EPD and the BLE protocol. This clinical promise also lies in the exclusive characteristics including real-time, continuous, range-controllable digital colorimetric displaying. Furthermore, this platform's compatibility with numerous existing electrochemical sensing technologies makes it promising for more practical and clinical applications as a next-generation wearable sweat sensor beyond paper-based colorimetry.

MATERIALS AND METHODS

Materials

TTF, glutaraldehyde, chitosan, acetic acid, PtB, PVC, tetrahydrofuran (THF), Nafion 117–containing solution, poly(pyromellitic dianhydride-*co*-4,4′-oxydianiline), amic acid solution, poly(vinyl pyrrolidone) (PVP), methanol, methyl methacrylate (MMA), 3-aminopropyltriethoxysilane (APTES), ethylene glycol dimethacrylate (EGDMA), 2,2′-azobis(2-methylpropionitrile) (AIBN) solution, methacrylic acid (MAA), toluene, SPAN 85, Halocarbon oil 27, oil blue N, sodium phosphate dibasic heptahydrate, sodium phosphate monobasic monohydrate, L-lactic acid, UA, D-glucose, sodium chloride, AA, urea, NH_4Cl, $CaCl_2$, and $MgCl_2$ were purchased from Sigma-Aldrich. LOx and buckypaper were obtained from Toyobo and NanoTechLabs, respectively. Titanium oxide nanopowder was acquired from AVENTION. The 495 PMMA A4 was purchased from Kayaku Advanced Materials. AZ5214E and AZ P4620 were obtained from AZ Electronic Materials. ISOPAR-G and ITO/glass were purchased from Exxonmobil chemical and Omniscience in order. KMPR 1010 was obtained from Microchem Inc. All chemicals except for MAA, EGDMA, and AIBN were all used without any purification. MMA, EGDMA, and AIBN were used after removal of the inhibitor by letting it flow through the inhibitor removal column.

Development of amperometric lactate sensor

To fabricate the electrodes for the oxygen-reductive cathode and lactate-oxidative anode, a connective rectangular-shaped trace comprising 150 nm of Au on a 15-nm Cr adhesion layer was transferred onto a FPCB covered with PDMS. To begin electrode transfer, poly(methyl methacrylate) (PMMA) solution was spin-coated at 3000 rpm for 30 s and baked at 180°C for 5 min to form a sacrificial layer. A layer of poly(pyromellitic dianhydride-*co*-4,4′-oxydianiline), amic acid solution was subsequently spin-coated at 4000 rpm for 30 s and baked at 250°C for 90 min to support the transferred Au electrode. Following the deposition of the Au and Cr layers, a typical etch-back process was used using an AZ5214E photoresist layer, defined by spin coating at 3000 rpm for 30 s, soft baking at 110°C for 1 min, 15 s of ultraviolet exposure, and 40 s of development. Photolithography using AZ4620 photoresist proceeded with similar conditions used for the previous process. AZ4620 was coated at 4000 rpm for 30 s followed by soft bake at 110°C for 3 min. Exposure of 1 min enabled defining the area of the exposed polyimide (PI) layer. After developing the photoresist with MIF500 for 110 s, areas where the PI layer was exposed were etched using O_2 reactive ion etching (RIE) at 150 W for 11 min. The remaining photoresist was removed, and the wafer was placed in boiling acetone at 60°C for approximately 4 hours to eliminate the sacrificial PMMA layer, allowing the Au electrode to be transferred to the PDMS substrate using a PDMS stamp treated with O_2 plasma.

For the fabrication of the circular sensitive areas to be connected to rectangular-shaped trace, 150 nm of Au on a 15-nm Cr adhesion layer was deposited on a PI film through e-beam evaporation. This layer was laser-cut into 2-mm-diameter circles to be used as a cathode or an anode. To immobilize LOx on the anode, buckypaper was used as the substrate, punched into 2-mm-diameter circles, and affixed to the Au using Ag paste. A solution of 2 μl of 0.1 M TTF in an acetone/ethanol mixture (1:9 volume ratio) and 4 μl of LOx solution (60 mg/ml in 0.01 M phosphate buffer of pH 7.4 with 0.25 wt % glutaraldehyde) was applied. Three microliters of chitosan solution was added to enhance the stability of the electrochemical sensor. The anode was further dipped into the same chitosan solution followed by a PVC solution (3% in THF). For the cathode, 6 μl of PtB in deionized water (10 mg/ml) was deposited on the circular Au electrode. A 0.4-μl drop of Nafion 117 solution was used to create an

immobilization layer. The 2-mm-diameter circular areas for both anode and cathode were connected to the previously mentioned connective trace using Ag paste, and this assembly was insulated using commercial epoxy.

Characterization of lactate amperometric sensor

The real-time voltage signal of lactate concentration was monitored using a potentiostat (PGSTAT204; Metrohm), while the electrochemical electrodes were immersed in a buffer solution. The temperature of the buffer was controlled by placing it on a hotplate, while the buffer was subjected to moderate stirring. To evaluate the reusability of the sensor, a cycle test was performed by promptly immersing the sensing electrodes into preheated 0 mM buffer. No additional washing process was required to obtain the cyclic response.

The artificial sweat used in the experiments was prepared according to a previous study (*10*). Twenty-two millimolar urea, 3 mM NH_4Cl, 0.4 mM $CaCl_2$, 50 μM $MgCl_2$, 25 μM UA, 0.1 mM glucose, and 5.5 mM lactic acid were used to prepare artificial sweat. The pH of the artificial sweat was adjusted to four different levels—7.5, 6.5, 5.5, and 4.5—to evaluate the pH dependence of the amperometric sensor's performance.

Fabrication of microfluidics for amperometric sensor

The microfluidic channel mold for the amperometric sensor was fabricated using the DRIE process. A layer of KMPR 1010 photoresist was spin-coated on a 4″ wafer at 3000 rpm for 30 s, achieving a thickness of approximately 11.3 μm. This was followed by a soft bake at 110°C for 5 min and exposure to a total of 420 mJ/cm^2, which enabled defining the deep trenches required for the microfluidic structures. Post exposure bake (PEB) at 100°C for 2 min further defined these structures. The development process using SU-8 developer for 2 min removed the unexposed regions of the photoresist, completing the mold.

The trenches achieved a depth of 600 μm through the DRIE process. Before casting PDMS mixed at a ratio of 10:1, a 150-nm layer of PMMA was deposited onto the mold. This PMMA layer, specifically PMMA 495 A4, was spin-coated at 3000 rpm and baked at 180°C for 5 min to facilitate the easier removal of the PDMS layer later. The PDMS solution was subsequently spin-coated on the mold at 200 rpm and cured at 180°C for several hours. Once cured, the microfluidic top layer was mechanically punched to create an outlet hole for sweat collection. This top layer, now featuring a hole, was bonded to the Au electrode–transferred PDMS substrate using O_2 plasma.

Preparation of E-ink

E-ink was prepared by dispersing pigment particles [TiO_2/P(MMA-EGDMA)-*co*-MAA] into a dyed oil suspension. The synthesis of pigment particles involves the following steps: TiO_2 core particles were treated with an APTES cross-linking agent to form TiO_2-APTES. Toluene was selected as the solvent for APTES functionalization. Refluxing 6.67 g of TiO_2 in a mixture of 351 ml of toluene and 17.6 ml of APTES for 12 hours (300 rpm, 65°C) enabled synthesis of APTES-functionalized TiO_2. Methanol was chosen as the solvent for the dispersion polymerization of TiO_2/P(MMA-EGDMA)-*co*-MAA. To prevent the aggregation of APTES-TiO_2 core particles, 12 g of PVP as a dispersant was introduced into 400 ml of methanol and stirred for 1 hour. After 20 min of sonication and stirring under N_2 following the addition of APTES-TiO_2, a sonicated mixture of monomers containing 15.2 ml of MMA and 724 μl of EGDMA was sequentially added. The synthesis was initiated by introducing 2184 μl of AIBN after the mixture was sonicated for 5 min. Dispersion polymerization was performed by refluxing the entire system for 25 hours at 250 rpm and 65°C. The charge control agent, MAA, was added during the reflux. Adequate washing and N_2 drying completed the preparation of the TiO_2/P(MMA-EGDMA)-*co*-MAA pigment particles for EPD.

The base oil solution was fabricated using Halocarbon oil 27 and ISOPAR-G. Oil blue N was added to this base oil mixture at a ratio of 0.14% (w/w), and the overall solution was sonicated for 1 hour to obtain a dyed oil suspension. The proportions of E-ink supplements were optimized to 12.6% (w/w) of synthesized pigment particles and 11.6% (w/w) of SPAN 85 of the total E-ink solution. Sonication of the total E-ink solution for approximately 5 min completed E-ink.

EPD fabrication

The detailed fabrication process of EPD is illustrated in fig. S3. Microfluidic chamber mold for E-ink injection was fabricated using a method similar to that used for an amperometric sensor. The patterning recipe for KMPR 1010 was identical to the one previously described. The thickness of the trench achieved via DRIE was 250 μm. The EPD spacer was constructed by pouring a mixture of elastomers (10:1 PDMS and Dragon Skin in a 3:4 ratio) onto a wafer mold. The ITO surface of the ITO/glass, which was electrically connected to the serpentine trace of the FPCB via Ag paste, was aligned with the wafer mold. Following the complete curing of the elastomer mixture, the inlet and the outlet were created using a mechanical punch, and the inside of the chamber was treated to display -NH_2 groups. The amine treatment was conducted by dropping APTES (1%) solution into the chamber for 5 min, followed by DI water rinsing. The completed EPD module was attached to the Cu electrode of the FPCB through O_2 plasma treatment, enabling the trapping of E-ink between the ITO top electrode and the Cu bottom electrode. E-ink was injected through the inlet using a pipette or a syringe.

Characterization of EPD

The performance of the EPD was characterized by CIELAB analysis. A video was recorded to analyze the EPD module while the driving waveform was applied. After capturing the video, it was converted into a series of pictures at an appropriate sampling rate. The RGB value of the EPD in each picture was obtained. The conversion of these RGB values to ΔE_{ab} involved a sequence of transformations: initially to linear RGB, subsequently to *XYZ*, followed by *xy*, and lastly to *L*a*b**.

The parameter of linear RGB was calculated as follows

$$(\text{linear } R) = \begin{cases} \dfrac{R'}{12.94} & (R \le 0.04045) \\ \left(\dfrac{R\prime + 0.055}{1.055}\right)^{2.4} & (R > 0.04045) \end{cases}$$

where R' is the portion of the R value obtained by $\frac{R}{255}$. The values of linear G and B were calculated similarly.

Parameters of X, Y, and Z could be defined by the following equation

$$X = \{(\text{linear } R) * 0.412453 + (\text{linear } G) * 0.35758 + (\text{linear } B) * 0.180423\} * 100$$

$$Y = \{(\text{linear } R) * 0.212671 + (\text{linear } G) * 0.71516 + (\text{linear } B) * 0.072169\} * 100$$

$$Z = \{(\text{linear } R) * 0.019334 + (\text{linear } G) * 0.119193 + (\text{linear } B) * 0.950227\} * 100$$

Next, the parameters of x and y were calculated as

$$x = \frac{X}{X + Y + Z}$$

$$y = \frac{Y}{X + Y + Z}$$

Finally, the value of x and y could be converted to L*a*b*

$$L* = 116 * f(Y/Y_n) - 16$$

$$a* = 500 * \left[f(X/X_n) - f(Y/Y_n)\right]$$

$$b* = 200 * \left[f(Y/Y_n) - f(Z/Z_n)\right]$$

To assess the change of color and response time of EPD, ΔE_{ab} was estimated as

$$\Delta E_{ab} = \sqrt{\Delta L*^2 + \Delta a*^2 + \Delta b*^2}$$

where $\Delta L*$, $\Delta a*$, and $\Delta b*$ indicate $L*_{white} - L*_{EPD}$, $a*_{white} - a*_{EPD}$, and $b*_{white} - b*_{EPD}$, respectively. $L*_{white}$, $a*_{white}$, and $b*_{white}$ were acquired similarly by analyzing the white reference point simultaneously.

Design and fabrication of the processing unit

Schematics of the FPCB and board layout were designed using AUTODESK EAGLE (version 9.6.2). The components include a Bluetooth SoC (nRF52832, Nordic Semiconductor), 32-MHz crystal (Q22FA1280002500, Epson Timing), 2.45-GHz antenna (2450AT18D0100E, Johanson Technology), 3.3-V power management integrated circuit (ADP160AUJZ-3.3-R7, Analog Devices Inc.), 3.7-V lithium polymer battery with an integrated battery protect circuit (220 mAh; TW651725, Thehan), slide switch (PCM12SMTR, C&K), color sensor (BU27006MUC-ZTR, ROHM Semiconductor), white LED (598-2A00-107F, Dialight), red LED (IN-S63ASR, Inolux), blue LED (IN-S63AS5B, Inolux), and passive elements with footprints of 0.6 mm × 0.3 mm (0201) and 1.0 mm × 0.5 mm (0402) (resistors, capacitors, and inductors). All components were assembled on the FPCB which was manufactured by a vendor using solder paste (SMDLTLFP, Chip Quik). Customized firmware was uploaded using Segger Embedded Studio (version 8.10b).

Processing of data in receive system

Processing unit transmitted data array including RGB parameter of pH paper, lactate molarity, and temperature via BLE notification. Customized application programmed by an MIT app inventor received the data array. Temperature and lactate molarity were updated on the graph once every second, and the scale of axes was automatically modified to help users recognize the physiological state. The application provided the collected data in CSV format for the precise postanalysis.

Human trial

Human trial was approved by Institutional Review Board of Korea university (KUIRB-2024-0020-01), and all experiments were conducted according to the approved protocol. The informed consent from all participants was obtained before the human trial. The EC device was attached onto the subject's forehead through a biocompatible double-sided tape (468MP, 3M). This double-sided tape had a microfluidic design established through a computer-aided design (CAD) program (Rhino, Robert McNeel & Associates). This design prevented sweat from accumulating under the device substrate and enabled more efficient collection of sweat. After the experiment, sweat was collected using an 1.5-ml tube, which was later analyzed using a commercial lactate sensor (Accutrend Plus, Roche).

Supplementary Materials

This PDF file includes:

Supplementary Text
Figs. S1 to S26
Tables S1 to S3
References

REFERENCES AND NOTES

1. L. Yin, M. Cao, K. N. Kim, M. Lin, J.-M. Moon, J. R. Sempionatto, J. Yu, R. Liu, C. Wicker, A. Trifonov, F. Zhang, H. Hu, J. R. Moreto, J. Go, S. Xu, J. Wang, A stretchable epidermal sweat sensing platform with an integrated printed battery and electrochromic display. *Nat. Electron.* **5**, 694–705 (2022).
2. S. Jo, D. Sung, S. Kim, J. Koo, A review of wearable biosensors for sweat analysis. *Biomed. Eng. Lett.* **11**, 117–129 (2021).
3. S. Kim, B. Lee, J. T. Reeder, S. H. Seo, S.-U. Lee, A. Hourlier-Fargette, J. Shin, Y. Sekine, H. Jeong, Y. S. Oh, A. J. Aranyosi, S. P. Lee, J. B. Model, G. Lee, M.-H. Seo, S. S. Kwak, S. Jo, G. Park, S. Han, I. Park, H.-I. Jung, R. Ghaffari, J. Koo, P. V. Braun, J. A. Rogers, Soft, skin-interfaced microfluidic systems with integrated immunoassays, fluorometric sensors, and impedance measurement capabilities. *Proc. Natl. Acad. Sci. U.S.A.* **117**, 27906–27915 (2020).
4. S. B. Kim, K. Lee, M. S. Raj, B. Lee, J. T. Reeder, J. Koo, A. Hourlier-Fargette, A. J. Bandodkar, S. M. Won, Y. Sekine, J. Choi, Y. Zhang, J. Yoon, B. H. Kim, Y. Yun, S. Lee, J. Shin, J. Kim, R. Ghaffari, J. A. Rogers, Soft, skin-interfaced microfluidic systems with wireless, battery-free electronics for digital, real-time tracking of sweat loss and electrolyte composition. *Small* **14**, e1802876 (2018).
5. W. Gao, S. Emaminejad, H. Y. Y. Nyein, S. Challa, K. Chen, A. Peck, H. M. Fahad, H. Ota, H. Shiraki, D. Kiriya, D.-H. Lien, G. A. Brooks, R. W. Davis, A. Javey, Fully integrated wearable sensor arrays for multiplexed in situ perspiration analysis. *Nature* **529**, 509–514 (2016).
6. Y. Wang, C. Zhao, J. Wang, X. Luo, L. Xie, S. Zhan, J. Kim, X. Wang, X. Liu, Y. Ying, Wearable plasmonic-metasurface sensor for noninvasive and universal molecular fingerprint detection on biointerfaces. *Sci. Adv.* **7**, eabe4553 (2021).
7. M. Wang, Y. Yang, J. Min, Y. Song, J. Tu, D. Mukasa, C. Ye, C. Xu, N. Heflin, J. S. McCune, T. K. Hsiai, Z. Li, W. Gao, A wearable electrochemical biosensor for the monitoring of metabolites and nutrients. *Nat. Biomed. Eng.* **6**, 1225–1235 (2022).
8. C. Ye, M. Wang, J. Min, R. Y. Tay, H. Lukas, J. R. Sempionatto, J. Li, C. Xu, W. Gao, A wearable aptamer nanobiosensor for non-invasive female hormone monitoring. *Nat. Nanotechnol.* **19**, 330–337 (2024).
9. L.-C. Tai, W. Gao, M. Chao, M. Bariya, Q. P. Ngo, Z. Shahpar, H. Y. Y. Nyein, H. Park, J. Sun, Y. Jung, E. Wu, H. M. Fahad, D.-H. Lien, H. Ota, G. Cho, A. Javey, Methylxanthine drug monitoring with wearable sweat sensors. *Adv. Mater.* **30**, 1707442 (2018).
10. Y. Sekine, S. B. Kim, Y. Zhang, A. J. Bandodkar, S. Xu, J. Choi, M. Irie, T. R. Ray, P. Kohli, N. Kozai, T. Sugita, Y. Wu, K. Lee, K.-T. Lee, R. Ghaffari, J. A. Rogers, A fluorometric skin-interfaced microfluidic device and smartphone imaging module for in situ quantitative analysis of sweat chemistry. *Lab Chip* **18**, 2178–2186 (2018).
11. E. H. Koh, W.-C. Lee, Y.-J. Choi, J.-I. Moon, J. Jang, S.-G. Park, J. Choo, D.-H. Kim, H. S. Jung, A wearable surface-enhanced Raman scattering sensor for label-free molecular detection. *ACS Appl. Mater. Interfaces* **13**, 3024–3032 (2021).

12. J. Tu, J. Min, Y. Song, C. Xu, J. Li, J. Moore, J. Hanson, E. Hu, T. Parimon, T.-Y. Wang, E. Davoodi, T.-F. Chou, P. Chen, J. J. Hsu, H. B. Rossiter, W. Gao, A wireless patch for the monitoring of C-reactive protein in sweat. *Nat. Biomed. Eng.* **7**, 1293–1306 (2023).
13. S. Anastasova, B. Crewther, P. Bembnowicz, V. Curto, H. M. Ip, B. Rosa, G.-Z. Yang, A wearable multisensing patch for continuous sweat monitoring. *Biosens. Bioelectron.* **93**, 139–145 (2017).
14. D.-H. Choi, J. S. Kim, G. R. Cutting, P. C. Searson, Wearable potentiometric chloride sweat sensor: The critical role of the salt bridge. *Anal. Chem.* **88**, 12241–12247 (2016).
15. K. Kwon, J. U. Kim, Y. Deng, S. R. Krishnan, J. Choi, H. Jang, K. Lee, C.-J. Su, I. Yoo, Y. Wu, L. Lipschultz, J.-H. Kim, T. S. Chung, D. Wu, Y. Park, T.-I. Kim, R. Ghaffari, S. Lee, Y. Huang, J. A. Rogers, An on-skin platform for wireless monitoring of flow rate, cumulative loss and temperature of sweat in real time. *Nat. Electron.* **4**, 302–312 (2021).
16. Y.-L. Liu, R. Liu, Y. Qin, Q.-F. Qiu, Z. Chen, S.-B. Cheng, W.-H. Huang, Flexible electrochemical urea sensor based on surface molecularly imprinted nanotubes for detection of human sweat. *Anal. Chem.* **90**, 13081–13087 (2018).
17. B. Wang, C. Zhao, Z. Wang, K.-A. Yang, X. Cheng, W. Liu, W. Yu, S. Lin, Y. Zhao, K. M. Cheung, H. Lin, H. Hojaiji, P. S. Weiss, M. N. Stojanović, A. J. Tomiyama, A. M. Andrews, S. Emaminejad, Wearable aptamer-field-effect transistor sensing system for noninvasive cortisol monitoring. *Sci. Adv.* **8**, eabk0967 (2022).
18. H. Y. Y. Nyein, M. Bariya, L. Kivimäki, S. Uusitalo, T. S. Liaw, E. Jansson, C. H. Ahn, J. A. Hangasky, J. Zhao, Y. Lin, T. Happonen, M. Chao, C. Liedert, Y. Zhao, L.-C. Tai, J. Hiltunen, A. Javey, Regional and correlative sweat analysis using high-throughput microfluidic sensing patches toward decoding sweat. *Sci. Adv.* **5**, eaaw9906 (2019).
19. H. Y. Y. Nyein, M. Bariya, B. Tran, C. H. Ahn, B. J. Brown, W. Ji, N. Davis, A. Javey, A wearable patch for continuous analysis of thermoregulatory sweat at rest. *Nat. Commun.* **12**, 1823 (2021).
20. J. R. Sempionatto, M. Lin, L. Yin, E. De la Paz, K. Pei, T. Sonsa-Ard, A. N. de Loyola Silva, A. A. Khorshed, F. Zhang, N. Tostado, S. Xu, J. Wang, An epidermal patch for the simultaneous monitoring of haemodynamic and metabolic biomarkers. *Nat. Biomed. Eng.* **5**, 737–748 (2021).
21. Y. Yang, Y. Song, X. Bo, J. Min, O. S. Pak, L. Zhu, M. Wang, J. Tu, A. Kogan, H. Zhang, T. K. Hsiai, Z. Li, W. Gao, A laser-engraved wearable sensor for sensitive detection of uric acid and tyrosine in sweat. *Nat. Biotechnol.* **38**, 217–224 (2020).
22. H. Gomez, J. A. Kellum, Lactate in sepsis. *JAMA* **313**, 194 (2015).
23. F. Gao, C. Liu, L. Zhang, T. Liu, Z. Wang, Z. Song, H. Cai, Z. Fang, J. Chen, J. Wang, M. Han, J. Wang, K. Lin, R. Wang, M. Li, Q. Mei, X. Ma, S. Liang, G. Gou, N. Xue, Wearable and flexible electrochemical sensors for sweat analysis: A review. *Microsyst. Nanoeng.* **9**, 1 (2023).
24. S. Emaminejad, W. Gao, E. Wu, Z. A. Davies, H. Y. Y. Nyein, S. Challa, S. P. Ryan, H. M. Fahad, K. Chen, Z. Shahpar, S. Talebi, C. Milla, A. Javey, R. W. Davis, Autonomous sweat extraction and analysis applied to cystic fibrosis and glucose monitoring using a fully integrated wearable platform. *Proc. Natl. Acad. Sci. U.S.A.* **114**, 4625–4630 (2017).
25. J. Kim, J. R. Sempionatto, S. Imani, M. C. Hartel, A. Barfidokht, G. Tang, A. S. Campbell, P. P. Mercier, J. Wang, Simultaneous monitoring of sweat and interstitial fluid using a single wearable biosensor platform. *Adv. Sci.* **5**, 1800880 (2018).
26. A. Koh, D. Kang, Y. Xue, S. Lee, R. M. Pielak, J. Kim, T. Hwang, S. Min, A. Banks, P. Bastien, M. C. Manco, L. Wang, K. R. Ammann, K.-I. Jang, P. Won, S. Han, R. Ghaffari, U. Paik, M. J. Slepian, G. Balooch, Y. Huang, J. A. Rogers, A soft, wearable microfluidic device for the capture, storage, and colorimetric sensing of sweat. *Sci. Transl. Med.* **8**, 366ra165 (2016).
27. A. J. Bandodkar, P. Gutruf, J. Choi, K. Lee, Y. Sekine, J. T. Reeder, W. J. Jeang, A. J. Aranyosi, S. P. Lee, J. B. Model, R. Ghaffari, C.-J. Su, J. P. Leshock, T. Ray, A. Verrillo, K. Thomas, V. Krishnamurthi, S. Han, J. Kim, S. Krishnan, T. Hang, J. A. Rogers, Battery-free, skin-interfaced microfluidic/electronic systems for simultaneous electrochemical, colorimetric, and volumetric analysis of sweat. *Sci. Adv.* **5**, eaav3294 (2019).
28. J. Choi, A. J. Bandodkar, J. T. Reeder, T. R. Ray, A. Turnquist, S. B. Kim, N. Nyberg, A. Hourlier-Fargette, J. B. Model, A. J. Aranyosi, S. Xu, R. Ghaffari, J. A. Rogers, Soft, skin-integrated multifunctional microfluidic systems for accurate colorimetric analysis of sweat biomarkers and temperature. *ACS Sens.* **4**, 379–388 (2019).
29. Y. Zhang, H. Guo, S. B. Kim, Y. Wu, D. Ostojich, S. H. Park, X. Wang, Z. Weng, R. Li, A. J. Bandodkar, Y. Sekine, J. Choi, S. Xu, S. Quaggin, R. Ghaffari, J. A. Rogers, Passive sweat collection and colorimetric analysis of biomarkers relevant to kidney disorders using a soft microfluidic system. *Lab Chip* **19**, 1545–1555 (2019).
30. S. B. Kim, Y. Zhang, S. M. Won, A. J. Bandodkar, Y. Sekine, Y. Xue, J. Koo, S. W. Harshman, J. A. Martin, J. M. Park, T. R. Ray, K. E. Crawford, K.-T. Lee, J. Choi, R. L. Pitsch, C. C. Grigsby, A. J. Strang, Y.-Y. Chen, S. Xu, J. Kim, A. Koh, J. S. Ha, Y. Huang, S. W. Kim, J. A. Rogers, Super-absorbent polymer valves and colorimetric chemistries for time-sequenced discrete sampling and chloride analysis of sweat via skin-mounted soft microfluidics. *Small* **14**, 1703334 (2018).
31. N. Mishra, N. T. Garland, K. A. Hewett, M. Shamsi, M. D. Dickey, A. J. Bandodkar, A soft wearable microfluidic patch with finger-actuated pumps and valves for on-demand, longitudinal, and multianalyte sweat sensing. *ACS Sens.* **7**, 3169–3180 (2022).
32. C.-H. Wu, H. J. H. Ma, P. Baessler, R. K. Balanay, T. R. Ray, Skin-interfaced microfluidic systems with spatially engineered 3D fluidics for sweat capture and analysis. *Sci. Adv.* **9**, eadg4272 (2023).
33. J. Kim, Y. Wu, H. Luan, D. S. Yang, D. Cho, S. S. Kwak, S. Liu, H. Ryu, R. Ghaffari, J. A. Rogers, A skin-interfaced, miniaturized microfluidic analysis and delivery system for colorimetric measurements of nutrients in sweat and supply of vitamins through the skin. *Adv. Sci.* **9**, 2103331 (2022).
34. J. T. Reeder, J. Choi, Y. Xue, P. Gutruf, J. Hanson, M. Liu, T. Ray, A. J. Bandodkar, R. Avila, W. Xia, S. Krishnan, S. Xu, K. Barnes, M. Pahnke, R. Ghaffari, Y. Huang, J. A. Rogers, Waterproof, electronics-enabled, epidermal microfluidic devices for sweat collection, biomarker analysis, and thermography in aquatic settings. *Sci. Adv.* **5**, eaau6356 (2019).
35. S. Krishnan, Z. u. Q. Syed, Colorimetric visual sensors for point-of-needs testing. *Sens. Actuators Rep.* **4**, 100078 (2022).
36. R. Celiesiute, A. Ramanaviciene, M. Gicevicius, A. Ramanavicius, Electrochromic sensors based on conducting polymers, metal oxides, and coordination complexes. *Crit. Rev. Anal. Chem.* **49**, 195–208 (2019).
37. G. Cai, J. Wang, P. S. Lee, Next-generation multifunctional electrochromic devices. *Acc. Chem. Res.* **49**, 1469–1476 (2016).
38. M. C. Hartel, D. Lee, P. S. Weiss, J. Wang, J. Kim, Resettable sweat-powered wearable electrochromic biosensor. *Biosens. Bioelectron.* **215**, 114565 (2022).
39. D. S. Kim, H. Lee, K. Keum, J. W. Kim, G. Jung, J. Kim, M. Park, J. Lee, H. Kang, S. J. Sim, J. S. Ha, A stretchable patch of multi-color electrochromic devices for driving integrated sensors and displaying bio-signals. *Nano Energy* **113**, 108607 (2023).
40. D. S. Kim, Y. H. Lee, J. W. Kim, H. Lee, G. Jung, J. S. Ha, A stretchable array of high-performance electrochromic devices for displaying skin-attached multi-sensor signals. *Chem. Eng. J.* **429**, 132289 (2022).
41. S. Santiago-Malagón, D. Río-Colín, H. Azizkhani, M. Aller-Pellitero, G. Guirado, F. J. Del Campo, A self-powered skin-patch electrochromic biosensor. *Biosens. Bioelectron.* **175**, 112879 (2021).
42. S. Inoue, H. Kawai, S. Kanbe, T. Saeki, T. Shimoda, High-resolution microencapsulated electrophoretic display (EPD) driven by poly-si TFTs with four-level grayscale. *IEEE Trans. Electron Devices.* **49**, 1532–1539 (2002).
43. D. Y. Kim, M.-J. Kim, G. Sung, J.-Y. Sun, Stretchable and reflective displays: Materials, technologies and strategies. *Nano Converg.* **6**, 21 (2019).
44. Z. Qiu, Z. Wu, M. Zhong, M. Yang, J. Xu, G. Zhang, Z. Qin, B.-R. Yang, Stretchable, washable, and rewritable electrophoretic displays with tough hydrogel–elastomer interface. *Adv. Mater. Technol.* **7**, 2100961 (2022).
45. Z. Qiu, Y. Gu, S. Zhu, Z. Wu, L. Peng, T. Wang, B.-R. Yang, Textile-based electrophoretic electronic paper displays with machine-washable, tailorable and thermostatic functions for truly wearable display. *SSRN Electron. J.* 10.2139/ssrn.4340890 (2023).
46. Z. Wang, H. Zhu, J. Zhuang, Y. Lu, Z. Chen, W. Guo, Recent advance in electrochromic materials and devices for display applications. *ChemPlusChem* **89**, e202300770 (2024).
47. C. Gu, A.-B. Jia, Y.-M. Zhang, S. X.-A. Zhang, Emerging electrochromic materials and devices for future displays. *Chem. Rev.* **122**, 14679–14721 (2022).
48. X. Xue, B. Liu, J. Hu, X. Bian, S. Lou, The potential mechanisms of lactate in mediating exercise-enhanced cognitive function: A dual role as an energy supply substrate and a signaling molecule. *Nutr. Metab.* **19**, 52 (2022).
49. M. G. Morris, H. Dawes, K. Howells, O. M. Scott, M. Cramp, Relationships between muscle fatigue characteristics and markers of endurance performance. *J. Sports Sci. Med.* **7**, 431–436 (2008).
50. D. Hansen, A. Abreu, M. Ambrosetti, V. Cornelissen, A. Gevaert, H. Kemps, J. A. Laukkanen, R. Pedretti, M. Simonenko, M. Wilhelm, C. H. Davos, W. Doehner, M.-C. Iliou, N. Kränkel, H. Völler, M. Piepoli, Exercise intensity assessment and prescription in cardiovascular rehabilitation and beyond: why and how: A position statement from the Secondary Prevention and Rehabilitation Section of the European Association of Preventive Cardiology. *Eur. J. Prev. Cardiol.* **29**, 230–245 (2022).
51. C. Gonçalves, A. Raimundo, A. Abreu, J. Bravo, Exercise intensity in patients with cardiovascular diseases: Systematic review with meta-analysis. *Int. J. Environ. Res. Public Health* **18**, 3574 (2021).
52. K. Goel, Q. R. Pack, B. Lahr, K. L. Greason, F. Lopez-Jimenez, R. W. Squires, Z. Zhang, R. J. Thomas, Cardiac rehabilitation is associated with reduced long-term mortality in patients undergoing combined heart valve and CABG surgery. *Eur. J. Prev. Cardiol.* **22**, 159–168 (2015).
53. G. O. Dibben, J. Faulkner, N. Oldridge, K. Rees, D. R. Thompson, A.-D. Zwisler, R. S. Taylor, Exercise-based cardiac rehabilitation for coronary heart disease: A meta-analysis. *Eur. Heart J.* **44**, 452–469 (2023).
54. S. Imani, A. J. Bandodkar, A. M. V. Mohan, R. Kumar, S. Yu, J. Wang, P. P. Mercier, A wearable chemical-electrophysiological hybrid biosensing system for real-time health and fitness monitoring. *Nat. Commun.* **7**, 11650 (2016).
55. X. Huang, J. Li, Y. Liu, T. Wong, J. Su, K. Yao, J. Zhou, Y. Huang, H. Li, D. Li, M. Wu, E. Song, S. Han, X. Yu, Epidermal self-powered sweat sensors for glucose and lactate monitoring. *Biodes. Manuf.* **5**, 201–209 (2022).

56. J. G. Pallarés, R. Morán-Navarro, J. F. Ortega, V. E. Fernández-Elías, R. Mora-Rodriguez, Validity and reliability of ventilatory and blood lactate thresholds in well-trained cyclists. *PLOS ONE* **11**, e0163389 (2016).
57. S. Kaufmann, T. Gronwald, F. Herold, O. Hoos, Heart rate variability-derived thresholds for exercise intensity prescription in endurance sports: A systematic review of interrelations and agreement with different ventilatory and blood lactate thresholds. *Sports Med. Open* **9**, 59 (2023).
58. M. E. Payne, A. Zamarayeva, V. I. Pister, N. A. D. Yamamoto, A. C. Arias, Printed, flexible lactate sensors: Design considerations before performing on-body measurements. *Sci. Rep.* **9**, 13720 (2019).
59. V. F. Curto, C. Fay, S. Coyle, R. Byrne, C. O'Toole, C. Barry, S. Hughes, N. Moyna, D. Diamond, F. Benito-Lopez, Real-time sweat pH monitoring based on a wearable chemical barcode micro-fluidic platform incorporating ionic liquids. *Sens. Actuators B Chem.* **171–172**, 1327–1334 (2012).
60. H. G. Menge, M. W. Kim, S. Lee, Y. T. Park, Silicone-based multifunctional thin films with improved triboelectric and sensing performances via chemically interfacial modification. *ACS Omega* **8**, 7135–7142 (2023).
61. A. L. Dalisa, Electrophoretic display technology. *IEEE Trans. Electron Devices.* **24**, 827–834 (1977).
62. K. Wnuczek, A. Puszka, Ł. Klapiszewski, B. Podkościelna, Preparation, thermal, and Thermo-mechanical characterization of polymeric blends based on Di(meth)acrylate monomers. *Polymers* **13**, 878 (2021).
63. H. Na, J. Baek, J. Kim, S. Kim, Preparation of charged composite particles for electrophoretic display. *Polymer* **33**, 347–352 (2009).
64. W. S. Mokrzycki, M. Tatol, Color difference Delta E—A survey. *Mach. Graph. Vis.* **20**, 383–411 (2011).
65. J. D. Wiles, S. R. Bird, J. Hopkins, M. Riley, Effect of caffeinated coffee on running speed, respiratory factors, blood lactate and perceived exertion during 1500-m treadmill running. *Br. J. Sports Med.* **26**, 116–120 (1992).
66. D. Jiang, C. Xu, Q. Zhang, Y. Ye, Y. Cai, K. Li, Y. Li, X. Huang, Y. Wang, In-situ preparation of lactate-sensing membrane for the noninvasive and wearable analysis of sweat. *Biosens. Bioelectron.* **210**, 114303 (2022).
67. X. Xuan, C. Chen, A. Molinero-Fernandez, E. Ekelund, D. Cardinale, M. Swarén, L. Wedholm, M. Cuartero, G. A. Crespo, Fully integrated wearable device for continuous sweat lactate monitoring in sports. *ACS Sens.* **8**, 2401–2409 (2023).
68. I. Shitanda, M. Mitsumoto, N. Loew, Y. Yoshihara, H. Watanabe, T. Mikawa, S. Tsujimura, M. Itagaki, M. Motosuke, Continuous sweat lactate monitoring system with integrated screen-printed MgO-templated carbon-lactate oxidase biosensor and microfluidic sweat collector. *Electrochim. Acta* **368**, 137620 (2021).
69. Y. Xu, E. De la Paz, A. Paul, K. Mahato, J. R. Sempionatto, N. Tostado, M. Lee, G. Hota, M. Lin, A. Uppal, W. Chen, S. Dua, L. Yin, B. L. Wuerstle, S. Deiss, P. Mercier, S. Xu, J. Wang, G. Cauwenberghs, In-ear integrated sensor array for the continuous monitoring of brain activity and of lactate in sweat. *Nat. Biomed. Eng.* **7**, 1307–1320 (2023).
70. R. Wang, Q. Zhai, T. An, S. Gong, W. Cheng, Stretchable gold fiber-based wearable textile electrochemical biosensor for lactate monitoring in sweat. *Talanta* **222**, 121484 (2021).

Acknowledgments

Funding: D.S. and J.Ko. were supported by the National Research Foundation of Korea (NRF) grant [RS-2024-00345402 and RS-2022-NR068227(2022M3H4A1A04098818)]. **Author contributions:** Conceptualization: D.S. and J.Ko. Methodology: D.S., S.H., Sumin Kim, and J.Ko. Investigation: D.S., S.H., Sumin Kim, Sungeun Kim, B.J., J.Ki., M.H., G.M., and Y.L. Discussion: H.K., G.K., and J.Ko. Visualization: D.S. Writing—original draft: D.S., S.H., Sumin Kim, and H.K. Writing—review and editing: D.S., J.Ko., S.-W.H., Y.-S.R., Sungbomg Kim, and H.J. Supervision: J.Ko. **Competing interests:** The authors declare that they have no competing interests. **Data and materials availability:** All data needed to evaluate the conclusions in the paper are present in the paper and/or the Supplementary Materials.

Submitted 30 October 2024
Accepted 24 February 2025
Published 28 March 2025
10.1126/sciadv.adu2142